Mid-infrared spectroscopy of the Andromeda galaxy

D. Hemachandra[1]⋆, P. Barmby[1], E. Peeters[1], S.P. Willner[2], M.L.N. Ashby[2], H.A. Smith[2], K.D. Gordon[3], D.A. Smith[3], and G.G. Fazio[2]

[1]*Department of Physics and Astronomy, University of Western Ontario, London, ON, N6A 3K7, Canada*
[2]*Harvard-Smithsonian Center for Astrophysics, Cambridge, MA 02138, USA*
[3]*Space Telescope Science Institute, 3700 San Martin Drive, Baltimore, MD 21218, USA*

ABSTRACT

We present *Spitzer*/Infrared Spectrograph 5–21 μm spectroscopic maps towards 12 regions in the Andromeda galaxy (M31). These regions include the nucleus, bulge, an active region in the star-forming ring, and 9 other regions chosen to cover a range of mid-to-far-infrared colours. PAH feature ratios (6.2 μm and 7.7 μm features compared to the 11.3 μm feature) measured from our extracted M31 spectra are consistent with these seen in other nearby galaxies. Our observations did not recover the unusual PAH ratios (suppressed 6–8 μm features and an enhanced 11.3 μm feature) seen in spectro-imaging observations with the ISOCAM instrument on the Infrared Space Observatory. The equivalent widths of the main PAH features decrease with increasing radiation hardness, consistent with that observed for other nearby spiral and starburst galaxies. The nucleus does not show any PAH emission except for the 11.3 μm feature, but does show strong silicate emission at 9.7 μm. Both of these characteristics provide evidence for a low luminosity active galactic nucleus in M31.

Key words: galaxies: individual: M31 – galaxies: ISM – galaxies: nuclei – infrared: ISM – ISM: molecules – ISM: lines and bands

1 INTRODUCTION

Mid-infrared spectra provide a unique diagnostic tool to understand the physical conditions in the interstellar medium of galaxies. The rich range of spectral features (Polycyclic Aromatic Hydrocarbons (PAHs), atomic fine structure lines (e.g. Ne, S) and the amorphous silicate feature centred at 9.7 μm) provide information on dust properties, radiation field and star formation. With the advent of infrared space telescopes, such as the Infrared Space Observatory (ISO, Kessler et al. 1996) and the *Spitzer* Space Telescope (Werner et al. 2004), we have been able to well explore the infrared emission from galaxies.

PAHs are known as the main carrier of the ubiquitous mid-IR emission bands (e.g. Allamandola et al. 1989, Tielens 2008). They are large hydrocarbon molecules consisting of ∼50–100 carbon atoms. The main PAH features are seen at 3.3, 6.2, 7.7, 8.6, 11.3 and 12.7 μm (e.g.Mattila et al. 1996, Peeters et al. 2002), and these bands are due to the vibrational de-excitation of PAH molecules through bending and stretching modes of C-H and C-C bonds (Tielens 2005). The 6 to 8 micron features are thought to originate mostly from ionized PAHs and the 3.3, 11.3, 12.7 and 17.1 μm emission bands from neutral PAHs (Peeters et al. 2002).

The relative strengths of the different PAH features do not vary much within normal-luminosity galaxies (Smith et al. 2007b) or within massive starburst galaxies (Brandl et al. 2006). However, feature ratios do change significantly close to active galactic nuclei where the overall strength of PAHs also gets weaker (Roche et al. 1991, Smith et al. 2007b). Smith et al. (2007b) found that the mid-IR spectra from weak AGNs show suppressed 6 to 8 μm PAH features but are bright at 11.3 μm. A possible explanation for this behaviour is that AGNs alter the grain composition by selective destruction of small ionized PAHs.

Previous studies of nearby galaxies indicate that metallicity and radiation hardness both affect PAH equivalent widths (EQWs). Smith et al. (2007b) and Engelbracht et al. (2008) showed that PAH EQWs in nearby star-forming galaxies decrease with increasing radiation hardness, although Brandl et al. (2006) found no such correlation within their starburst sample. With metallicity, PAH EQWs show an anti-correlation in star-forming galaxies (Marble et al. 2010). This variation of PAHs among galaxies has also been observed within H II regions of a single galaxy (M101) by Gordon et al. (2008). But there are no other investigations done on a single star-forming galaxy with sufficiently high resolution to see whether the correlations mentioned above hold within a galaxy similar to the Milky Way.

The amorphous silicate feature at 9.7 μm is another as-

⋆ E-mail: dhemacha@uwo.ca

pect of the mid-IR spectra of galaxies and in particular their nuclei. Spoon et al. (2007) classified infrared galaxies based on the equivalent width of the 6.2 μm PAH feature and the strength of the 9.7 μm silicate feature. They found galaxies spread along two distinct branches: one in which silicate absorption strength was anti-correlated with PAH equivalent width, and another in which the weak silicate feature strength did not depend on the 6.2 μm equivalent width. Silicate *emission* at 9.7 μm has also been observed in both Seyfert 1 and Seyfert 2 galaxies and can be used to constrain the geometry and structure of the emitting nuclear region (Mason et al. 2009). While M31's nucleus is known to be rather inactive from an X–ray perspective (Li et al. 2011), mid-infrared indicators of its nuclear activity, such as silicate absorption or emission, have received relatively little attention. The higher spatial resolution available in observations of a very nearby galaxy like M31, compared to luminous, distant objects such as ultra-luminous infrared galaxies (Spoon et al. 2007) or nearby Seyferts (Mason et al. 2009), makes exploring its mid-infrared spectrum worthwhile.

M31 with its proximity ($\sim$780 kpc) and rich observational databases provides the most detailed view of a star forming galaxy similar to the Milky Way. The active star forming ring visible in 8 μm *Spitzer*/IRAC images (Barmby et al. 2006) provides evidence of abundant PAHs in M31. However, ISOCAM spectro-imaging observations of M31(Cesarsky et al. 1998) showed that four regions including the nucleus and bulge of this galaxy have very odd PAH spectra, bright at 11.3 and 12.7 μm but lacking the usual 6.2, 7.7, and 8.6 micron bands. Investigating this unusual PAH emission was the main motivation for the work described in this paper. We employed mid-IR spectral maps from the *Spitzer*/Infrared Spectrograph (IRS) from 12 regions of M31 for a further investigation of its infrared properties. This sample includes the nucleus, bulge, an active region in the star-forming ring (all previously observed by ISOCAM), and 9 other regions chosen to cover a range of properties as described in Section 2.1. We obtained the processed version of ISOCAM observations of M31 and compare them with the IRS results in Section 3.1. Section 4.1 discusses PAH intensity ratios. In Section 4.2, we investigate the relationship between PAH equivalent widths and radiation hardness and compare to that found by Engelbracht et al. (2008) and Gordon et al. (2008). Metallicity and PAH EQWs are compared in Section 4.3, and Section 4.4 discusses the dust properties of the nucleus.

2   OBSERVATIONS AND DATA REDUCTION

2.1   IRS observations

We obtained mid-infrared spectral maps of 12 regions in M31 using the *Spitzer*/IRS instrument (Houck et al. 2004) covering wavelengths from 5 to 21 microns. These regions include the nucleus, two regions previously observed by ISOCAM, and 9 other regions chosen to cover a range of UV intensities, metallicities and dust temperatures. Dust temperatures were determined using an $8 - 24/70 - 160$ μm colour-colour diagram (see Figure 1). The locations of the observed regions are shown in Figure 2, and their coordinates are given in Table 1. The two regions previously observed by ISOCAM
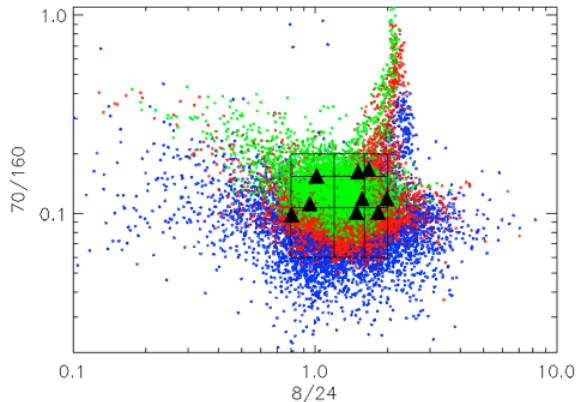

Figure 1. $8 - 24/70 - 160$ μm colour-colour diagram of M31 obtained from IRAC and MIPS. The plot is divided into 9 regions (black grid) and the observations were made to cover those regions. The triangles indicate the regions we observed. (**Needs a better explanation**)

are the region from the bulge and the region from the active region in the star-forming ring (Region 9 in our sample). A background observation was also made off the galaxy along the minor axis and it was used to enable the background subtraction from the data cubes.

For our observations we used the IRS Short-Low (SL) and Long-Low (LL) modules which cover wavelengths from 5 to 21 microns. The Low modules have resolving power in the range 60–130. Each low-resolution module is divided into two sub-slits which provide spectroscopy in either first or second order. They are denoted as SL1 (7.5–14.5 μm), SL2 (5.2–7.6 μm), LL1 (20.5–38.5 μm, not used in these observations), and LL2 (14.5–20.75 μm). All M31 regions were observed in September 2007 as part of G. G. Fazio's Guaranteed Time (program ID 40032). The map size was based on the size of the IRS slits (SL: $3.6'' \times 57''$, LL: $10.5'' \times 168''$). Each region was covered by 18 overlapping observations of the SL slit and 11 overlapping observations of the LL slit making the map size $32'' \times 57''$ for SL and $58'' \times 168''$ for LL. Figure 3 shows an example of the slit arrangement. For the brighter regions (nucleus, bulge), ramp times of 14 s (SL) and 30 s (LL) were used, while for the fainter regions, ramp times of 60 and 120 s were used respectively. Background observations were taken with each module (2 per ramp time). Since all of the targets are in the same part of the sky, a common background observation was used for multiple targets to subtract the background emission.

2.2   IRS Data Reduction

The data were reduced through the SSC pipeline (ver. S17.2.0) and the maps were assembled using the CUBISM program (Smith et al. 2007a). Bad pixel removal was also done using CUBISM and the background observations were used to subtract the background emission from these cubes following the method outlined in Gordon et al. (2008). Spectra were extracted using a $30'' \times 50''$ rectangular aperture. The aperture size was selected to cover the overlapping area of the SL and LL modes; all the IRS maps cover additional area than is considered here.

Table 1. Spitzer/IRS Target Locations in M31

Name	R.A. (J2000)	Decl. (J2000)	$R_{\rm gc}{}^{b}$	$12 + \log({\rm O/H})$
Nucleus[a]	$00^{\rm h}42^{\rm m}44^{\rm s}\!.31$	$41°16'09''\!.4$	0.0	
Bulge[a]	$00^{\rm h}42^{\rm m}35^{\rm s}\!.00$	$41°21'01''\!.0$	4.7	8.90 ± 0.03
Region 1	$00^{\rm h}41^{\rm m}30^{\rm s}\!.41$	$40°43'07''\!.8$	12.4	9.20 ± 0.20
Region 2	$00^{\rm h}45^{\rm m}22^{\rm s}\!.85$	$41°38'53''\!.1$	13.0	9.07 ± 0.02
Region 3	$00^{\rm h}40^{\rm m}37^{\rm s}\!.37$	$41°01'29''\!.4$	12.1	8.85 ± 0.01
Region 4	$00^{\rm h}41^{\rm m}17^{\rm s}\!.86$	$41°07'09''\!.8$	8.7	8.89 ± 0.06
Region 5	$00^{\rm h}43^{\rm m}39^{\rm s}\!.57$	$41°19'03''\!.1$	7.0	8.93 ± 0.08^{c}
Region 6	$00^{\rm h}43^{\rm m}35^{\rm s}\!.72$	$41°23'15''\!.0$	4.3	8.73 ± 0.08
Region 7	$00^{\rm h}40^{\rm m}53^{\rm s}\!.98$	$40°58'58''\!.9$	8.7	8.40 ± 0.08
Region 8	$00^{\rm h}42^{\rm m}21^{\rm s}\!.60$	$41°07'17''\!.4$	3.1	8.94 ± 0.08^{c}
Region 9[a]	$00^{\rm h}41^{\rm m}00^{\rm s}\!.00$	$40°36'20''\!.3$	13.5	8.86 ± 0.02
NGC 206	$00^{\rm h}40^{\rm m}20^{\rm s}\!.20$	$40°44'54''\!.0$	9.8	
Background	$00^{\rm h}44^{\rm m}41^{\rm s}\!.80$	$40°58'56''\!.0$	29.5	

[a]Regions with ISOCAM data.
[b]De-projected galactocentric distance, in kpc
[c]Metallicity values obtained from the radial metallicity profile of M31.
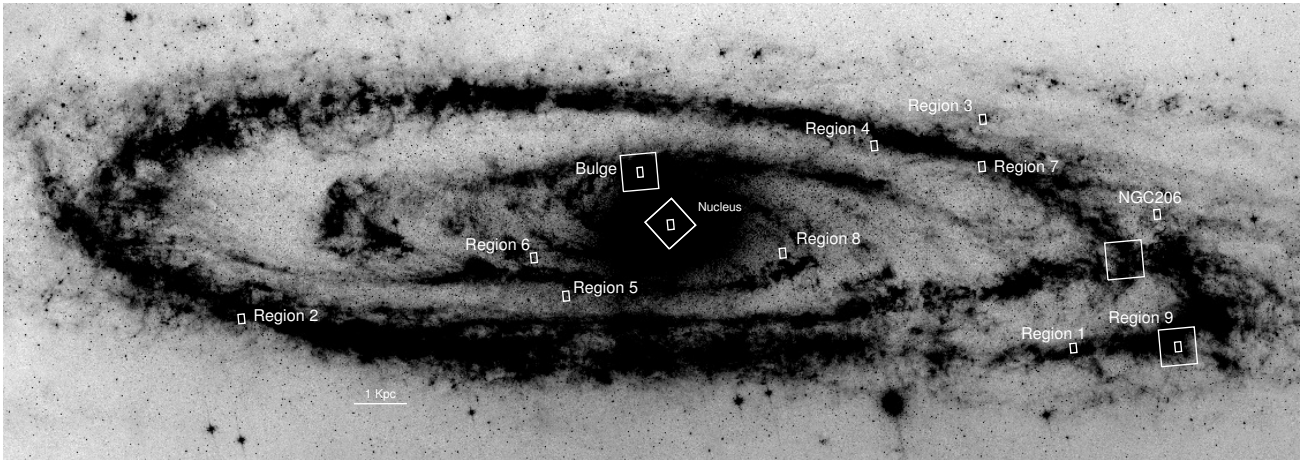
Figure 2. An 8 micron IRAC image of M31 (Barmby et al. 2006). Small white rectangles ($30'' \times 50''$) show the regions that we observed and larger squares ($192'' \times 192''$) show the regions observed by Cesarsky et al. (1998).

After the spectral extraction there was a noticeable mismatch between the spectra from the SL1 and LL2 modules. To combine all spectra to obtain one spectrum, first a photometric comparison was conducted between the IRS spectra and the IRAC 8 μm image of M31 (Barmby et al. 2006). (For more details about this method see the IRAC Instrument Handbook Section 4.) Fluxes from the IRAC image were extracted using the same apertures as for spectral extraction, and the extended source aperture correction of 0.824 applied The uncertainty of the IRAC photometry was estimated by taking the standard deviation of pixel values within an aperture of the same size from a position off the galaxy (00:48:58.00, +42:14:54.00).

Then we stitched the SL1 and SL2 using the overlapping regions and applied a colour correction factor K, which is a multiplicative factor that converts the intensity of an IRS spectrum at a given wavelength to the intensity of an IRAC image taken at the same wavelength. We used the IDL code provided by the instrument handbook to compute these K values for all the regions. Colour correction values and the corresponding IRS data along with the IRAC data are given

in Table 2. It was observed that the spectrum from the NGC 206 is very noisy, therefore that spectrum was removed from our analysis.

Figure 4 compares the IRS and IRAC 8 μm photometry. The line of best fit weighted by the uncertainties has a slope of 0.81 ± 0.08 and intercept of -0.05 ± 0.06. Since the intercept in Figure 4 is not zero with a higher uncertainty, it can be concluded that the offsets between orders are due to an additive offset than a multiplicative offset. Also an additive offset favours more for stitching SL and LL modes. Based on this argument, first we shifted the combined SL1 and SL2 spectrum so that the intensity at 8 μm matches with that of IRAC 8 micron image. To do this shift, the following equation was used to find the offset values (x) between IRS and IRAC image intensities at 8 microns.

$$F_{IRAC8} = [F_{IRS8} + x] \times K \qquad (1)$$

K is the colour correction factor, F_{IRAC8} is the intensity of the IRAC 8 μm image (aperture corrected) and F_{IRS8} is the intensity of IRS spectra at 8 μm. The offsets for all the regions are listed in Table 2. After that the LL2 mode was

Table 2. Matched aperture photometry

Name	IRS Intensity at 8 μm[a]	IRAC Intensity at 8 μm[a]	colour K[b]	x[a, c]
Region 1	1.8505	1.3923	0.532	0.3061
Region 2	1.8238	1.3731	0.555	0.2148
Region 3	0.7192	0.9689	0.767	0.3218
Region 4	1.1431	0.8513	0.589	0.0407
Region 5	0.6787	0.8088	0.773	0.1834
Region 6	0.6399	0.7656	0.927	0.0479
Region 7	1.1538	0.8243	0.526	0.1380
Region 8	0.5556	0.7135	0.877	0.1148
Region 9	1.9413	1.6562	0.606	0.3107
Bulge	2.6956	2.5473	0.532	1.2425

[a]Units are MJy sr^{-1}. [b]Colour correction factors [c]Offset between IRAC and IRS as mentioned in eq. 1. Intensities are given prior to the extended source correction and the colour correction.

Figure 4. Intensity of the aperture corrected IRAC 8 μm image vs that of the colour corrected IRS spectra at 8 μm obtained using the same aperture for our regions in M31. The straight line is the line of best fit.

Figure 3. SL1 data cube from the nucleus showing the arrangement of slits used to cover the region. A black box outlines the footprint of the short-low maps and the green box outlines the LL2. Blue and red slits show how each map was covered using overlapping slit positions.

CAM data is shown in Figure 5. For the three regions, we extracted spectra using the same $30'' \times 50''$ aperture as for the IRS data.

stitched by shifting it towards the SL1 by an amount of the average difference in their overlapping spectral regions.

2.3   ISOCAM Data Reduction

To compare our results with those of Cesarsky et al. (1998), we retrieved the highly processed ISOCAM data provided by Boulanger et al. (2005) for the three regions in common. The ISOCAM data were obtained with the circular variable filters (CVFs) over a $3' \times 3'$ field of view at a scale of $6''$ per pixel. The wavelength range covered was 5.15–16.5 μm at a resolution of $\lambda/\Delta\lambda \approx 45$; the ISOCAM instrument is described by Cesarsky et al. (1996). An image of the ISO-
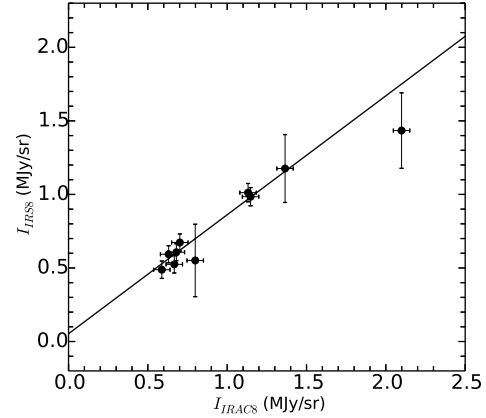
3   ISOCAM COMPARISON AND SPECTRAL FEATURE MEASUREMENT

The final processed IRS spectra are shown in Figure 6. All of the main PAH features, including the 6.2, 7.7, 8.6 and 11.3 μm bands, are clearly visible for all the regions except the nucleus. (The spectrum of the nucleus is discussed in Section 4.3.) The IRS spectra also show atomic line emission such as [Ar II], [Ar III], [S III], [S IV], [Ne II], [Ne III] and molecular H_2 emission at 12.3 μm. Some of the spectra display a contribution to the continuum from starlight emission.
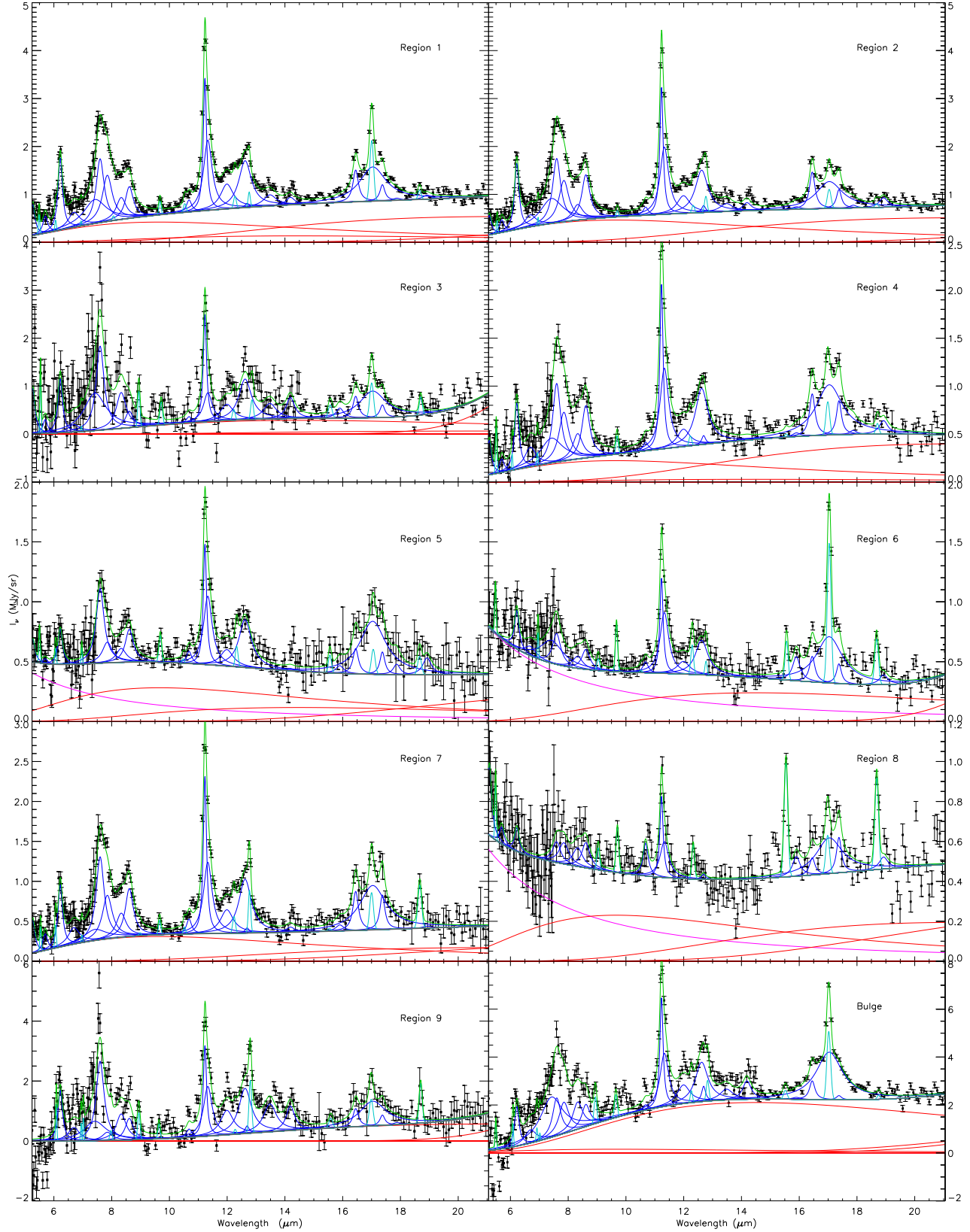
Figure 6. Observed IRS spectra and detailed PAHFIT decompositions (see Section 3.2). Regions are labeled in each panel. Black squares show the observed data, and red, blue, light blue, pink and green lines represent the modelled dust continua, PAH features, atomic lines, starlight continuum and the fit respectively. The black line shows the total modelled continuum. Vertical scales differ in different panels. Spectra from the nucleus and NGC 206 are not shown here.

Table 3. PAH Emission Line Strengths[a]

Region	5.7μm	6.2μm	7.7μm	8.3μm	8.6μm	10.7μm	11.3μm	12.0μm	12.7μm	17.0μm
Region 1	10±1	34±1-09	107±10	13±1	14.1±0.9	2.2±0.3	33.4±0.9	9.1±0.5	16±1	17±1
Region 2	7.7±0.9	31.2±0.8	106±8	9±1	19.8±0.8	1.5±0.2	32.0±0.8	6.6±0.4	15±1	14.7±0.9
Region 3	8±4	25±3	111±22	21±4	7±3	1.1±0.9	19±3	6±1	14±3	13±2
Region 4	4±1	15.8±0.9	59±9	7±1	11.6±0.8	0.8±0.2	19.9±0.8	3.5±0.4	9±1	12.5±0.9
Region 5	1±1	7±1	22±3	3±1	5.8±0.8	0.9±0.2	12.7±0.8	2.4±0.4	6.3±0.4	10±2
Region 6	- - - -	7.3±0.9	22±7	3±1	3.6±0.8	0.8±0.2	10.8±0.8	1.9±0.4	4.5±0.4	8.3±0.6
Region 7	5.9±0.9	17.7±0.9	57±8	9±1	12.8±0.8	1.6±0.2	21.8±0.8	5.2±0.4	11±1	13±2
Region 8	2.±1	3±1	6±3	3±1	2.7±0.8	1.4±0.3	4.4±0.8	- - - -	- - - -	4.1±0.7
Region 9	- - - -	38±3	133±29	25±4	15±3	2.4±0.8	37±3	14±1	25±3	19±6
Bulge	- - - -	38±2	219±27	32±4	20±3	2.0±0.9	53±3	14±1	29±3	39±2

[a] Units are 10^{-9} W m^{-2}.

Table 4. PAH Emission Line Equivalent Widths[a]

Name	5.7μm	6.2μm	7.7μm	8.3μm	8.6μm	10.7μm	11.3μm	12.0μm	12.7μm	17.0μm
Region 1	0.39±0.08	1.2±0.1	3.4±0.3	0.43±0.04	0.47±0.04	0.09±0.01	1.45±0.04	0.43±0.03	0.78±0.03	1.27±0.05
Region 2	0.28±0.04	1.02±0.06	3.4±0.2	0.32±0.04	0.70±0.04	0.07±0.01	1.58±0.04	0.35±0.02	0.85±0.03	1.35±0.06
Region 3[b]	4±2	8±2	19±4	2.8±0.8	0.9±0.5	0.1±0.1	2.1±0.3	0.7±0.2	1.6±0.2	2.4±0.3
Region 4	0.28±0.09	1.0±0.1	3.7±0.4	0.5±0.1	0.77±0.07	0.07±0.02	1.67±0.06	0.31±0.04	0.86±0.05	1.68±0.07
Region 5	- - - -	0.12±0.03	0.61±0.08	0.10±0.03	0.20±0.03	0.05±0.01	0.77±0.03	0.17±0.03	0.50±0.04	1.6±0.2
Region 6	- - - -	0.10±0.04	0.6±0.2	0.10±0.04	0.14±0.03	0.05±0.01	0.77±0.04	0.15±0.03	0.42±0.04	1.7±0.1
Region 7	0.32±0.05	0.86±0.06	2.8±0.2	0.44±0.06	0.69±0.06	0.12±0.02	1.81±0.07	0.48±0.05	1.11±0.08	2.2±0.2
Region 8	0.03±0.04	0.04±0.03	0.2±0.10	0.09±0.04	0.10±0.03	0.09±0.02	0.30±0.02	0.00±0.00	0.01±0.01	0.62±0.07
Region 9[b]	- - - -	237±100	151±60	16±6	8±3	0.5±0.2	7±1	2.3±0.6	3.6±0.8	2.4±0.8
Bulge	- - - -	1.2±0.2	4.0±0.4	0.51±0.07	0.30±0.06	0.03±0.01	0.78±0.03	0.22±0.02	0.49±0.03	1.16±0.04

[a] Units are μm. [b] Continuum for these regions is very weak. Equivalent widths are highly uncertain and not considered in the analysis (see Section 3).
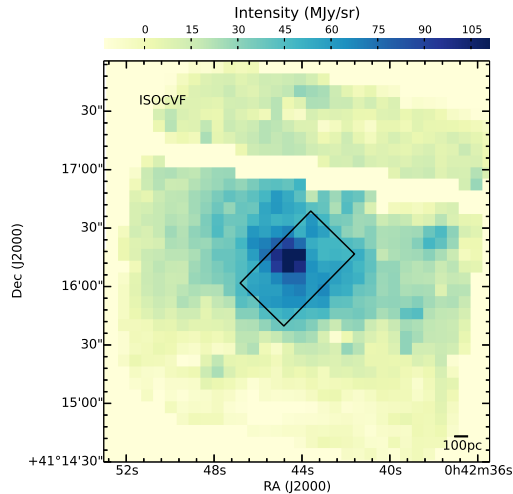
Figure 5. 11.3 μm negative image of the ISOCAM data cube from the nucleus of M31. The black box shows the size of the aperture ($30'' \times 50''$) used to extract spectra.

3.1 ISOCAM versus IRS

As mentioned in the Introduction, based on ISOCAM observations Cesarsky et al. (1998) reported a suppression of the common 6 to 8 μm features and an enhancement of a broad 11.3 and 12.7 μm features in four regions of M31. In addition,

Pagani et al. (1999) confirmed that the star-forming ring in M31 shows very weak PAH emission in the 6 to 8 μm region. However, the IRS spectra presented here do not show such unusual behaviour (Figure 6). Indeed, except for the nucleus, all regions show a normal mid-infrared spectrum similar to other nearby starforming galaxies. Therefore, we obtained newly-processed ISOCAM spectra from three regions in our IRS sample (see Section 2.3) and compared them with the corresponding IRS spectra. Figure 7 shows that although the feature relative intensities in the IRS and ISOCAM spectra differ in detail, the shapes of the spectra are almost identical. Except for the nucleus, there is no depletion in 6 to 8 μm features as described by Cesarsky et al. (1998).

Until 2005, ISOCAM data were not properly background subtracted and they were contaminated with zodiacal emission and stray light. Differential spectra between regions of relatively strong and weak emission were previously used to overcome this problem (more details about the differential spectra are given by Cesarsky et al. 1998). In 2005, the ISOCAM data were reprocessed and corrected for the zodiacal emission (Boulanger et al. 2005). It is clear that the spectra obtained from these newly processed ISOCAM data do not agree with the previous differential spectra, especially for the bulge and the nucleus. Indeed, the differential spectrum shows a broad emission feature around the 11.3 μm feature not visible in Figure 7 (top). Also, the differential spectrum towards the bulge does not show any emission in the 6 to 8 μm spectral region, unlike the newly processed data (Figure 7 middle). The new ISOCAM reduction ap-

Table 5. Atomic Emission Line Strengths[a]

Name	[Ar II] 7.0μm	[Ar III] 9.0μm	[S IV] 10.5μm	[Ne II] 12.8μm	[Ne III] 15.5μm	[S III] 18.7μm
Region 1	<15.2	<16.4	6±1	6±1	< 4.2	2.2±0.4
Region 2	5±3	< 17.4	<5.1	6±1	< 2.9	0.9±0.5
Region 3	<42.9	27±6	< 28.9	9±3	6±1	4.3±0.9
Region 4	<11.2	<10.0	<4.4	2±1	0.6±0.5	1.3±0.5
Region 5	4±3	<6.2	< 5.2	< 4.2	2±1	2±1
Region 6	7±3	4±2	< 3.8	2±1	5.4±0.5	5.3±0.5
Region 7	3±3	<12.6	2.3±0.9	10±2	< 2.9	8±1
Region 8	<11.8	5±2	<4.9	<2.6	11.6±0.5	6.5±0.5
Region 9	24±10	35±8	< 2.7	38±3	7±4	15.3±5.6
Bulge	10±7	49±7	< 30.4	19±4	7±2	2±1

[a]Units are 10^{-10} W m^{-2}. Upper limits are indicated with a < mark.
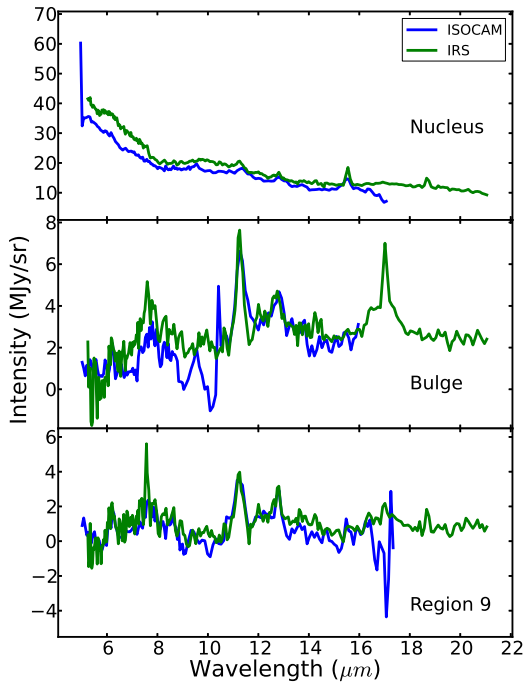
Figure 7. Comparison of IRS and re-processed ISOCAM spectra for the Nucleus (top), Bulge (middle) and Region 9 (bottom) in M31.

pears to eliminate the discrepancies between ISOCAM and IRS, resulting in less 'strange' infrared spectra for M31. For the remainder of this work, we discuss only the IRS spectra.

3.2 PAHFIT

The PAH features in the IRS spectra are often blended with neighbouring aromatic features and atomic lines. Therefore measuring the strength of PAH features is difficult. To achieve this task a tool called PAHFIT, introduced by Smith et al. (2007b), was used. PAHFIT is an IDL based tool designed for decomposing *Spitzer* IRS low-resolution spectra of PAH emission sources and is capable of identifying PAH fea-

tures among other blended features. It also takes silicate absorption and extinction into account. PAHFIT uses six main components to fit the surface brightness. These are starlight continuum, featureless thermal dust continuum, pure rotational lines of H_2, fine-structure lines, dust emission features and dust extinction. The starlight is represented by blackbody emission at a fixed temperature of 5000 K and the dust continuum is represented by 8 modified blackbodies (emissivity proportional to ν^2) at fixed temperatures of 35, 40, 50, 65, 90, 135, 200, and 300 K. The final fit obtained with PAHFIT does not necessarily use all eight dust components. The infrared extinction is considered as a combination of a power law plus silicate absorption features with peaks at 9.7 and 18 μm. Line features are represented by Gaussian profiles with widths set by the instrumental resolution and dust features are represented by Drude profiles; more details about PAHFIT are given by Smith et al. (2007b).

Initial attempts at fitting the spectra with PAHFIT showed that some components were negligible, and to avoid over-fitting we re-ran the fits without these components. None of the IRS spectra shows significant silicate absorption around 9.7 or 18 μm and the extinction values calculated by PAHFIT in the initial fits were almost zero. Except for four regions (the bulge, Region 5, Region 6 and Region 8), the starlight contribution is also negligible. We adjusted the PAHFIT input parameters to fix extinction to zero for all regions and starlight to zero for all but the four regions above. Typically only two or three thermal dust components had significant power in our fits, but we did not fix the unused components to zero. Regions 3 and 9 were found to have very low dust continuum emission compared to other spectra, possibly because of noisy data at short wavelengths. However the other features in these spectra appear to be fit correctly. The spectrum of the nucleus shows silicate emission (see Section 4.4), which is not included in PAHFIT; consequently PAHFIT was unable to sucessfuly fit the other spectral features in this spectrum.

3.3 PAH features

PAHFIT returns fluxes and equivalent widths (EQWs) of PAH features which are given in Tables 3 and 4. The intensities of the features do not include any contribution from the continuum but the equivalent width computed by
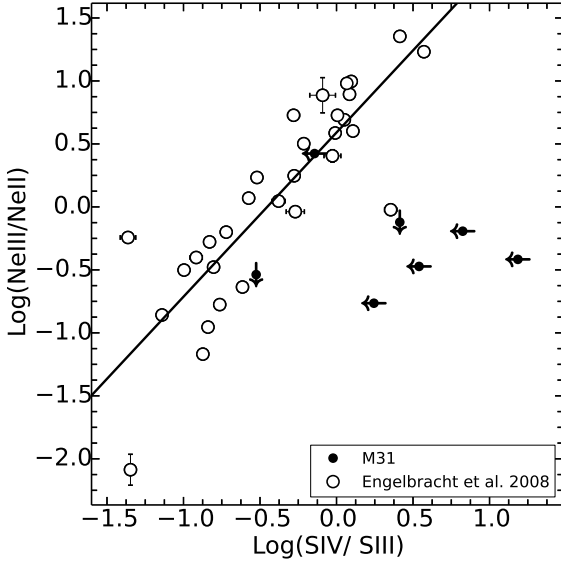
Figure 8. Log([Ne III]/[Ne II]) vs Log([S IV]/[S III]) 18 for the M31 regions in our sample (black dots) and for the starburst sample from Engelbracht et al. (2008) (open dots). The straight line is the line of best fit for the starburst sample.

$$\text{EQW} = \int \frac{I_\nu - I_{\nu,\text{cont}}}{I_{\nu,\text{cont}}} \, d\lambda, \tag{2}$$

is a measure of both the strength of the continuum emission ($I_{\nu,\text{cont}}$) and the line strength ($I_{\nu,\text{feature}}$). Here $I_\nu = I_{\nu,\text{feature}} + I_{\nu,\text{cont}}$. The continuum emission is mainly coming from ordinary dust grains, much larger than PAH molecules. Hence, by studying EQWs of PAHs, we can study how the PAHs compete with the dust grains in the mid-infrared wavelengths. PAHFIT returns the EQW values for each PAH feature and the uncertainties were calculated using a Monte-Carlo method. In that method, for each region, PAH-FIT was run 500 times on randomly generated data points normally distributed within the uncertainties of the spectrum. PAHFIT returned 500 EQW values for each PAH feature and the standard deviation of EQWs for a given feature was taken as its uncertainty. The EQWs from Regions 3 and 9 were removed from further analysis because the negligible dust continuum for these spectra makes the EQWs highly uncertain.

3.4 Atomic line features

PAHFIT also returns the emission line strengths and the flux uncertainties of atomic lines. These are listed in Table 5. Line ratios of [Ne III]/[Ne II] and [S IV]/[S III] 18 have been used as an indication of the radiation hardness. Engelbracht et al. (2008) demonstrated that a combination of these two line ratios -which they call the radiation hardness index (RHI)- is a more sensitive indicator of the hardness of the radiation. The RHI values are calculated using

$$\text{RHI} = \left(\log \frac{[\text{Ne III}]}{[\text{Ne II}]} + [0.71 + 1.58 \log \frac{[\text{S IV}]}{[\text{S IV}]}] \right) / 2 \tag{3}$$

Here, 1.58 and 0.71 are the slope and the intercept of the [Ne III]/[Ne II] vs [S IV]/[S III] 18 plot (Figure 8) for the starburst sample from Engelbracht et al. (2008). The RHI has also been used by Gordon et al. (2008) for M101 observations. To investigate whether the atomic line emission from the selected regions of M31 with the fit parameters described above, we compared them to the starburst sample (Figure 8).

We calculated upper limits for non-detected lines [1]. Figure 8 shows that the limits are reasonably following the trend for the starburst galaxy sample. Therefore the equation mentioned above was adopted with a simple modification to calculate the RHI values for our sample. For the regions with missing Ne lines, equation 4 was used and for the regions with missing S lines, equation 5 was used.

$$\text{RHI} = 0.71 + 1.58 \log \frac{[\text{S IV}]}{[\text{S III}]} \tag{4}$$

$$\text{RHI} = \log \frac{[\text{Ne III}]}{[\text{Ne II}]} \tag{5}$$

For Regions 2, 5, and 8, we used the upper limit values of their atomic line intensities to calculated RHI values.

4 RESULTS AND DISCUSSION

4.1 PAH intensities

Both the 6.2 and 7.7 μm features are thought to be coming from ionized PAHs and the 11.3 μm feature is from neutral PAHs. Therefore we expect to see a correlation between the intensities of 6.2 and 7.7 μm PAH features normalized by the 11.3 μm feature. In Figure 9 we compare the PAH flux ratios of 7.7/11.3 and 6.2/11.3 features. The figure shows a good correlation between these two PAH line ratios and is consistent with that of SINGS sample shown by Smith et al. (2007b). This correlation has also been reported in Galliano et al. (2008) and Vermeij et al. (2002). This provides evidence that the PAH emission from M31 is not unusual.

4.2 Aromatic equivalent widths versus radiation hardness

As mentioned in the introduction, aromatic equivalent widths tend to show an inverse correlation with radiation hardness. We used the radiation hardness index (RHI) values calculated using the method described in Section 3.4 to study how the EQW values from our sample agree with this. The equivalent widths of the PAH features are compared with RHI in Figures 10 and 11. For reference, we have added this to the starburst sample of Engelbracht et al. (2008) and the H II regions in M101 of Gordon et al. (2008). The equivalent widths seems to be decreasing with increasing radiation hardness, consistent with previous results. This also helps to confirm that the aromatic emission in M31 is not unusual.

Atomic line intensities depend on the distance from H II

---

[1] To find the upper limits for the flux of missing atomic lines, we assumed the line to be a Gaussian profile with a FWHM as given by PAHFIT. The peak intensity was taken to be 3 times the RMS, where RMS is the root mean square of the noise at the position of a missing line.
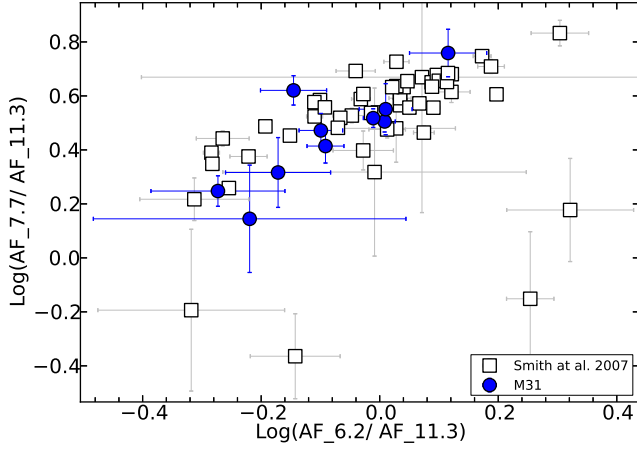
Figure 9. Flux ratios for PAH features (7.7/11.3 versus 6.2/11.3) for 10 regions in M31.
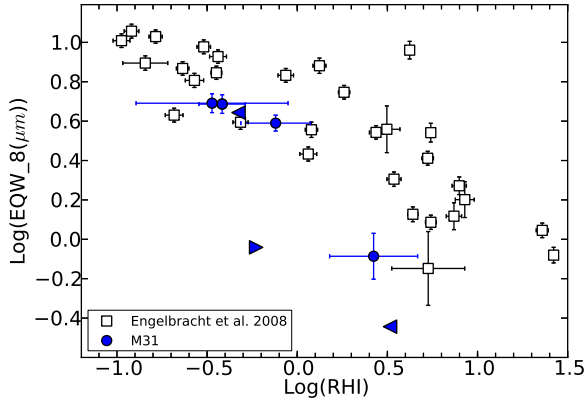

Figure 10. Equivalent widths of the 8 μm aromatic feature versus radiation hardness index (RHI) for the M31 sample (blue). Open squares represent the starburst sample from Engelbracht et al. (2008). Here the 8μm feature is a combination of the 7.7, 8.3 and 8.6 μm PAHFIT components. Triangles represents the upper and lower limits.

region to the extraction region used to obtain a spectrum (Stock et al. 2014, in prep.). For example, [Ne II] line intensity can be higher from an extraction close to the H II region than from an extraction further away. Our maps are at different distances from H II regions. Therefore the calculated RHI values must have been affected by this.

4.3   Aromatic equivalent widths versus metallicity

Many studies based on ISO and *Spitzer* observations have reported that PAH intensity decreases with decreasing metallicity (Calzetti et al. 2010). In addition, these studies also report a sudden drop of EQWs of PAHs around $12 + \log{(O/H)} \approx 8.1$. This has been observed amongst different galaxies (Engelbracht et al. 2008) as well as within a single galaxy (Gordon et al. 2008).

Here we investigate the relation between the PAH features and the metallicity for the M31 regions in this paper.
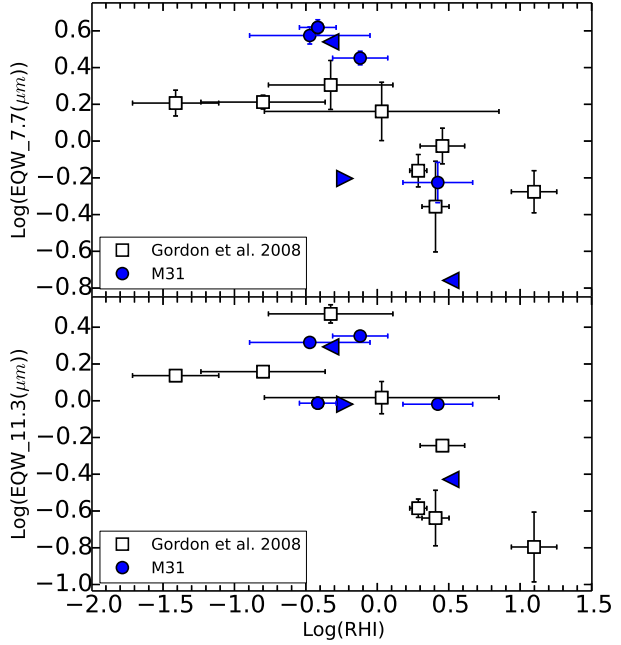

Figure 11. Equivalent widths of the normalized 7.7 μm aromatic feature (top panel) and 11.3 μm aromatic feature (bottom panel) versus radiation hardness index (RHI) for the M31 sample. Open squares represent the data from M101 by Gordon et al. (2008). The normalization was done by dividing each EQW by the weighted average over all regions in the respective samples. Triangles are the upper and lower limits.

Sanders et al. (2012) provided metallicities for more than 250 H II regions and this catalogue was used to find the metallicity values for the regions of interest in this paper. Except for two regions (Region 5, Region 8), we found the metallicity values for all the regions under the strong line diagnostic method of N06 N2 described in Sanders et al. (2012). This method uses [N II]/Hα and [O III]/[N II] oxygen abundance calibrations of Nagao et al. 2006. Sanders et al. (2012) also provided a radial metallicity profile of M31 based on the N06 N2 method which we used to find metallicity values for Region 5 and Region 8. Our regions do not cover metallicity values less than 8.40 (see Table 1).

The normalized EQWs of the PAH features are plotted versus the metallicity in our sample and the starburst galaxies of Engelbracht et al. (2008) in Figure 12. The metallicities in Engelbracht's work have been obtained by the direct electron temperature method (Skillman et al. 1998) whereas we used N06 N2 method. There is an offset between the metallicities generated by these two methods since the N06 N2 method gives slightly higher values for the metallicity than the direct method. This offset has been calculated by Croley et al. (2014) to be 0.35±0.10. In Figure 12 we have corrected for this offset by subtracting 0.35 from our metallicity values.

Equivalent widths of the 7.7 and 11.3 μm features are not inconsistent with those of Engelbracht et al. (2008). However, we do not have enough data from low-metallicity regions in M31 to observe the expected decrease of EQWs of PAH with the decreasing metallicity. There do seem to be some outliers which can plausibly be due to the uncertain-
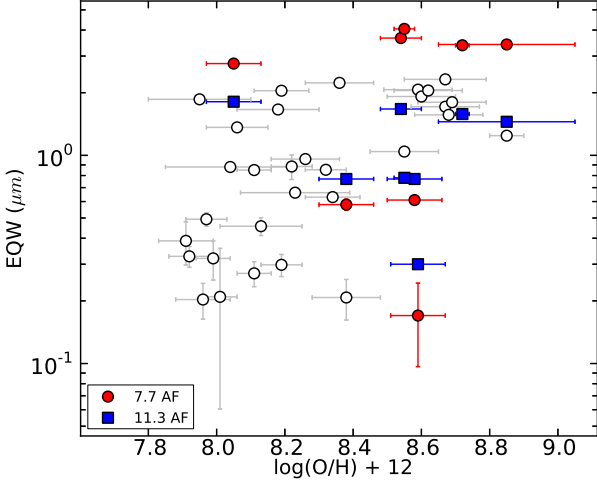
Figure 12. PAH equivalent widths versus metallicity. EQWs of the 7.7 μm feature of the starburst sample from Engelbracht et al. (2008) are plotted in open circles.
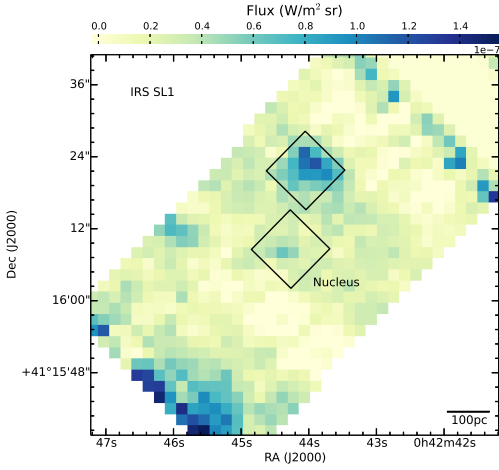

Figure 13. Intensity variation of 11.3 μm emission around the nucleus of M31. Two black boxes are the apertures (centre and north region) used to extract spectra in Figure 14. The centre of the nucleus is at R.A. 0h42m44.35s, Dec. +41d16m08.5s (Garcia et al. 2010).

ties and the offset between different methods of calculating the metallicity.

4.4   Dust properties of the nucleus

The centre of M31 has a complicated physical structure. It hosts a very inactive supermassive black hole with a mass of $0.7 - 1.4 \times 10^8$ M$_\odot$ (Bacon et al. 2001) and it also has a lopsided nuclear disk (Lauer et al. 1993) with two stellar components and an A-star cluster. The spectra of the nucleus from both *Spitzer* and ISOCAM show similar characteristics in the mid infrared wavelengths. Emission from the nucleus is missing the most common 6 to 8 μm PAH features while showing considerable emission around 11.3 μm.

A suppression of 6 to 8 μm features has also been observed in other nearby star-forming galaxies with a low-luminosity AGN (Smith et al. 2007b). One explanation for this behaviour is that the AGN environment can selectively destroy the ionized or small PAH molecules which contribute to the 6 to 8 μm features (whereas larger, neutral PAHs contribute to the 11.3 μm feature). Another argument is that the AGN is unrelated or partially responsible for the PAH spectra alterations. Smith et al. (2007b) argue that this variation could be used to detect weak AGNs in dusty galaxies where optical diagnostics are not available. In Figure 14 we compare the spectrum of the nucleus of M31 with spectra extracted close to the nucleus of 6 other nearby galaxies and they all look very similar. All six galaxies are known to have low luminosity AGNs (LLAGNs) in the centre. Since M31 is showing a similar spectrum from the nucleus we can infer that M31 also has a weak AGN at the centre.

Figure 13 shows the integrated intensity map of 11.3 μm emission around the nucleus. It can be observed that the majority of the 11.3 μm emission is coming from two regions (North and South East) around the centre of the nucleus and not from the centre. To study this further, we extracted two spectra, one from the centre and one from the North region using a 5×5 pixel square aperture as shown in Figure 13. The spectrum extracted from the North region shows a strong 11.3 μm peak as expected and no considerable emission from 6 to 8 μm features (Figure 14, inset). On the other hand the centre shows no PAH emission (Figure 14) but silicate emission around 9.7 μm which is not present in the North spectrum. To investigate whether there are any other regions that show silicate emission close to the nucleus, a continuum subtracted image was produced which shows the 9–11 μm integrated silicate emission intensity (see Figure 15). This silicate emission map shows that only the exact centre of the nucleus contributes to the silicate emission.

Spoon et al. (2007) report that galaxies which have AGN activity show silicate emission around 9.7 μm. In the unified model of AGNs, an edge on view through cool dust (type 2 AGNs) in the torus causes silicate absorption whereas a face-on view (type 1 AGNs) shows silicate emission (Efstathiou & Rowan-Robinson 1995). The latter could be the reason for silicate emission of M31 if it holds a Seyfert-like AGN. But the mid-IR spectra do not contain forbidden atomic lines such as [Ne V] and [S IV] which are indicative of such an active nucleus (Spinoglio & Malkan 1992).

Alternatively, the silicate emission is not directly associated with the torus but rather originate in the optically thin hot dust around the torus (Mason et al. 2012). The first detection of such silicate emission is reported in Sturm et al. (2005) from the low-ionization nuclear emission-line region (LINER) galaxy NGC 3998. LINERs are powered by accretion onto massive black holes and due to the low accretion rates these are classified as the low-luminosity AGNs (Kewley et al. 2006). Mason et al. 2012 has observed that this 9.7 μm silicate emission is present in many LLAGNs. They also have explained that these objects cannot host a Seyfert-like obscuring torus because of their optically thin dust and low dust-to-gas ratio. By taking all these into account, we can suggest that M31 hosts a low-luminosity AGN.

Also, the bolometric luminosity of the nucleus was calculated to be (value goes here erg/ s) using the 12 μm flux
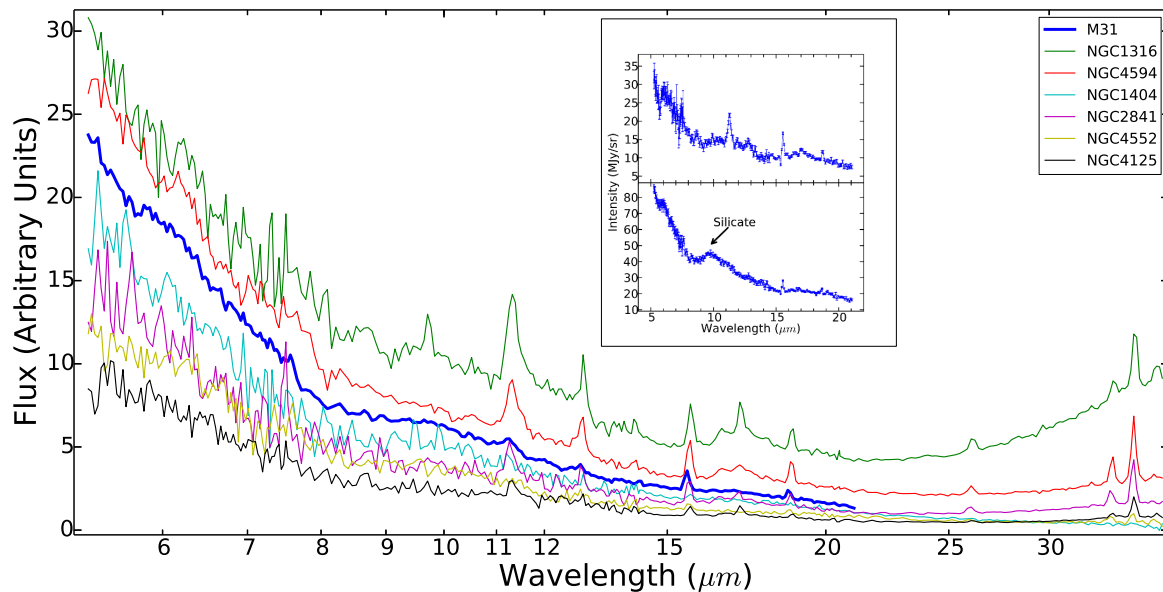
Figure 14. Mid-infrared spectrum of the nucleus of M31 (blue) over-plotted with spectra extracted close to the nuclei of 6 nearby galaxies which have AGN activity (Smith et al. 2007b). NGC 4552, NGC 1404 and NGC 4125 are elliptical galaxies and NGC 4594 and NGC 2841 are spiral galaxies. NGC 1316 is a lenticular galaxy. The inset shows the spectra extracted from the centre region of the M31 nucleus (bottom) and from the north region (top) shown in Figure 13.
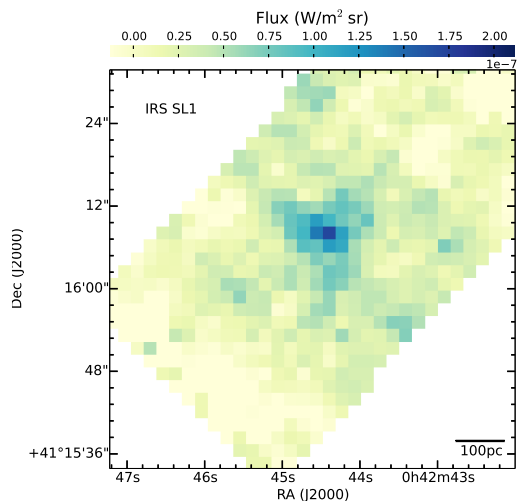

Figure 15. The integrated strength of the silicate emission (from 9 to 11 μm) near the M31 nucleus.

using the method described in Spinoglio & Malkan (1989). This value is closer to that of other LLAGNs.

5   SUMMARY AND CONCLUSIONS

We have obtained *Spitzer*/IRS spectral maps of 12 regions of M31 covering wavelengths 5–21 μm. The spectra from those regions, except the nucleus, agree with spectra obtained from other nearby star forming galaxies. However, they are inconsistent with previous ISOCAM observations of M31 (Cesarsky et al. 1998) reporting a suppression of the 6–8 μm features and an enhancement of 11.3 μm fea-

ture towards 4 regions. Our IRS spectra for three of these ISOCAM regions do not show this unusual behaviour. ISO-CAM data corresponding to those three regions in common between our study and that of (Cesarsky et al. 1998) were obtained from the ISO archive. These data were reprocessed in 2005 to remove contamination by stray light and zodiacal emission; spectra extracted from these newly processed data could not reproduce previous results. Therefore we conclude that the earlier results based on ISOCAM data were affected by the background subtraction methods applied to overcome the contamination.

The equivalent widths of PAH features in M31 regions showed a decreasing trend with increasing radiation hardness, consistent with previous results from other nearby galaxies. The PAH EQWs versus metallicity data points were well within the values from the starburst galaxy sample of Engelbracht et al. (2008). We did not have enough data from low-metallicity regions of M31 to observe the decreasing trend of EQWs at low metallicity values which is visible in other galaxies.

The mid-infrared spectrum from the nucleus was compared with that of six other galaxies which are known to have AGN activity. All have a similar spectral shape and present suppressed 6–8 μm features and a strong 11.3 μm feature. Smith et al. 2007b says that this type of spectrum can be used to identify a low luminosity AGN. Therefore we argue that the centre of M31 hosts a low-luminosity AGN, supporting that argument. The spectrum obtained from the centre region of the nucleus had a strong silicate emission around 9.7 μm which is also evidence for the presence of a low-luminosity AGN.

ACKNOWLEDGEMENTS

REFERENCES

Allamandola L. J., Tielens A. G. G. M., Barker J. R., 1989, ApJS, 71, 733

Bacon R., Emsellem E., Combes F., Copin Y., Monnet G., Martin P., 2001, A&A, 371, 409

Barmby P., et al., 2006, ApJ, 650, L45

Boulanger F., et al., 2005, A&A, 436, 1151

Brandl B. R., et al., 2006, ApJ, 653, 1129

Calzetti D., et al., 2010, Conference Proceedings 'Reionization to Exoplanets', ed. P. Ogle, ASP Conference Series,

Cesarsky C. J., et al., 1996, A&A, 315, L32

Cesarsky D., Lequeux J., Pagani L., Ryter C., Loinard L., Sauvage M., 1998, A&A, 337, L35

Croley M., Barmby P., Stock D., Azimlu M., Rosolowsky E., 2014, MNRAS, submitted

Efstathiou A., Rowan-Robinson M., 1995, MNRAS, 273, 649

Engelbracht C. W., Rieke G. H., Gordon K. D., Smith J.-D. T., Werner M. W., Moustakas J., Willmer C. N. A., Vanzi L., 2008, ApJ, 678, 804

Galliano F., Madden S. C., Tielens A. G. G. M., Peeters E., Jones A. P., 2008, ApJ, 679, 310

Garcia M. R., et al., 2010, ApJ, 710, 755

Gordon K. D., Engelbracht C. W., Rieke G. H., Misselt K. A., Smith J.-D. T., Kennicutt Jr. R. C., 2008, ApJ, 682, 336

Houck J. R., et al., 2004, ApJS, 154, 18

Kessler M. F., et al., 1996, A&A, 315, L27

Kewley L. J., Groves B., Kauffmann G., Heckman T., 2006, MNRAS, 372, 961

Lauer T. R., et al., 1993, AJ, 106, 1436

Li Z., Garcia M. R., Forman W. R., Jones C., Kraft R. P., Lal D. V., Murray S. S., Wang Q. D., 2011, ApJ, 728, L10

Marble A. R., et al., 2010, ApJ, 715, 506

Mason R. E., Levenson N. A., Shi Y., Packham C., Gorjian V., Cleary K., Rhee J., Werner M., 2009, ApJ, 693, L136

Mason R. E., et al., 2012, AJ, 144, 11

Mattila K., Lemke D., Haikala L. K., Laureijs R. J., Leger A., Lehtinen K., Leinert C., Mezger P. G., 1996, A&A, 315, L353

Nagao T., Maiolino R., Marconi A., 2006, A&A, 459, 85

Pagani L., Lequeux J., Cesarsky D., Milliard B., Lionard L., Sauvage M., 1999, A&A, 351, 447

Peeters E., Hony S., Van Kerckhoven C., Tielens A. G. G. M., Allamandola L. J., Hudgins D. M., Bauschlicher C. W., 2002, A&A, 390, 1089

Roche P. F., Aitken D. K., Smith C. H., Ward M. J., 1991, MNRAS, 248, 606

Sanders N. E., Caldwell N., McDowell J., Harding P., 2012, ApJ, 758, 133

Skillman E. D., Terlevich E., Terlevich R., 1998, Space Sci. Rev., 84, 105

Smith J.-D. T., et al., 2007a, PASP, 119, 1133

Smith J.-D. T., et al., 2007b, ApJ, 656, 770

Spinoglio L., Malkan M. A., 1989, ApJ, 342, 83

Spinoglio L., Malkan M. A., 1992, ApJ, 399, 504

Spoon H. W. W., Marshall J. A., Houck J. R., Elitzur M., Hao L., Armus L., Brandl B. R., Charmandaris V., 2007, ApJ, 654, L49

Stock D., Peeters E., Choi W., Shannon M., 2014, ApJ, in press

Sturm E., et al., 2005, ApJ, 629, L21

Tielens A. G. G. M., 2005, The Physics and Chemistry of the Interstellar Medium. Cambridge University Press, Cambridge, UK

Tielens A. G. G. M., 2008, ARA&A, 46, 289

Vermeij R., Peeters E., Tielens A. G. G. M., van der Hulst J. M., 2002, A&A, 382, 1042

Werner M. W., et al., 2004, ApJS, 154, 1

This paper has been typeset from a TeX/ LaTeX file prepared by the author.